Thermo-fluid-metallurgical modelling of laser-based powder bed fusion process

Bayat, Mohamad; Mohanty, Sankhya; Hattel, Jesper H.

Publication date:
2018

Document Version
Peer reviewed version

Thermo-fluid-metallurgical modelling of laser-based powder bed fusion process

Mohamad Bayat[1,*], Sankhya Mohanty[1], Jesper. H. Hattel[2]

[a] Department of Mechanical Engineering, DTU, building 425, room 225, Lyngby, Denmark

[*] Corresponding author

Introduction

Selective laser melting (SLM) is a type of additive manufacturing (AM) technique where the parts are produced in a layer-wised manner. In this process, first a layer of fine metallic spherical particles, with sizes spanning from 20-50 µm, is distributed over a rigid building platform whose elevation can be readily adjusted while the part is being manufactured [1]. When the first powder layer is distributed, a laser with a typical spot size of about 30-100 µm starts scanning it. The input heat imposed from the laser is sufficiently high to melt down and subsequently fuse these discrete particles together. After the first layer has been scanned, the building table (containing the part) moves one increment down and then another powder layer will be distributed with the same coating mechanism. This process is repeated until the final part is manufactured [2].

SLM has many advantages over other conventional production methods such has casting, milling, forging, etc. These are the possibility of complex designs, low material waste and short total manufacturing process time [3]. Although SLM is regarded as a superior technique to some of the existing conventional manufacturing processes, it still needs to be modified to an extent that it becomes more predictable. To address this issue and predict the quality of the parts produced by SLM, one can make use of numerical modelling.

Numerical models, especially if validated with experimental measurements, can be used as an easy and cheap way to predict the feature and quality of the SLM parts. In this respect, different numerical models containing different physics have been developed for the SLM process, ranging from pure thermal models [4], [5] to thermo-mechanical models [6] and the more advanced meso-scale thermo-fluid models [7], [8]. Consideration of just the conductive heat transfer is a proven and well-tested way of SLM modelling. In this type of models, a moving heat source or heat flux, resembles the laser-material interaction. On the other hand, thermal models including the fluid flow, despite incurring much more computational time, will give detailed information about the actual melt pool thermal history, its morphology and even its eventual microstructure [7], [9].

In this work, a thermo-fluid-metallurgical model of the SLM process for a titanium alloy has been developed to analyze the thermal and fluid behavior of the molten metal inside the melt pool. The model takes into account the Marangoni effect caused by the change in shear stresses. To thermally and fluid-mechanically model the solidification phenomenon, the enthalpy-porosity method and solidification drag forces in the porous medium are implemented respectively. Furthermore, an additional microstructural model has been developed and subsequently coupled to the mentioned model to investigate the solidification behavior of the melt pool. In this respect, the important solidification data, such as solidification cooling rate, morphology factor, growth velocity and solidification thermal gradient are calculated during the solidification as well.

Numerical model

To find the velocity field of the liquid metal during the SLM process, it is necessary to solve the coupled partial differential equations of balance of mass (namely continuity) and linear momentum.

$$\boldsymbol{\nabla}.\boldsymbol{V} = 0, \tag{1}$$

$$\rho[\boldsymbol{V}_t + \boldsymbol{V}.\boldsymbol{\nabla}(\boldsymbol{V})] = -\boldsymbol{\nabla}P + \boldsymbol{\nabla}.\tau_{ij} + \boldsymbol{F}_V, \tag{2}$$

$$\tau_{ij} = 2\mu\left[\frac{1}{2}\left(V_{i,j} + V_{j,i}\right) - \frac{1}{3}V_{k,k}\delta_{ij}\right]. \tag{3}$$

The ρ $[\frac{kg}{m^3}]$ and $\boldsymbol{V}$ $[\frac{m}{s}]$ in equations (1) and (2) are density and the velocity vector respectively. The τ_{ij} [Pa] in equation (3) is the internal viscous stress tensor for a laminar incompressible fluid flow. To model the effect of solidification of the fluid flow, the volumetric solidification drag forces have been implemented which are functions of velocity and liquid fraction of the fluid (metal) [10].

$$\boldsymbol{F}_V = -c\frac{(1-f_l)^2}{B+f_l^3}.\boldsymbol{V} + \rho\boldsymbol{g}\beta(T - T_l). \tag{4}$$

The two parameters c $\left[\frac{\text{kg}}{\text{m}^3.\text{s}}\right]$ and B $[-]$ in equation (4) are the Carman-Kozeny constants, which, depending on the application, are in the range of $10^5 - 10^7$and $10^{-5} - 10^{-3}$ respectively. The role of the B $[-]$ is to prevent the denominator becoming absolute zero. f_l $[-]$ in equation (4) is the liquid fraction of the metal. According to this equation, when the solidification begins, the liquid fraction becomes smaller and in this case, the volume forces increase dramatically. In the extreme case of total solidification where the liquid fraction becomes zero, the volume forces become so big in magnitude that they effectively freeze the fluid flow in the corresponding regions. On the other hand, when the liquid fraction becomes unity, the solidification drag forces disappear, hence they free the fluid. The last term on the right hand side of equation (4) is the buoyancy force. Since the flow is assumed to be incompressible in this work, the Boussinesq approximation has been used to account for the buoyancy effect. β $\left[\frac{1}{K}\right]$ and $\boldsymbol{g}$ are thermal expansion coefficient and gravity acceleration vector respectively.

The partial differential equation of balance of heat must be solved to find the temperature distribution of the computational domain.

$$\rho[h_t + \boldsymbol{V}.\boldsymbol{\nabla}h] = \boldsymbol{\nabla}.[k\boldsymbol{\nabla}T] + \dot{Q}'''. \qquad (5)$$

The widely-used enthalpy-porosity method has been implemented to solve equation (5). h $[\frac{kJ}{kg}]$, k $\left[\frac{W}{m.K}\right]$ and $\dot{Q}'''$ $[\frac{W}{m^3}]$ are specific enthalpy, thermal conductivity and heat generation source term respectively. The liquid fraction used for the thermal analysis is assumed to be a linear function of temperature.

$$f_l = \begin{cases} 0 & ,T < T_s \\ \dfrac{T - T_s}{T_l - T_s} & ,T_s < T < T_l \\ 1 & ,T_l < T, \end{cases} \qquad (6)$$

$$h = h_{ref} + \int_{T=T_{amb}}^{T} C_p dT + f_l \Delta H_{sl}. \qquad (7)$$

In the equations (6) and (7), T_s $[K]$ and T_l $[K]$ are solidus and liquid temperatures respectively. h_{ref} $[\frac{kJ}{kg}]$ is the reference enthalpy and ΔH_{sl} $[\frac{kJ}{kg}]$ is the latent heat of the fusion.

Since the powder has an initial porosity of ϕ, the mass-average method has been used to find the thermo-physical properties of the powder layer.

$$c_{p,powder} = \frac{[1-\varphi]c_{p_s}\rho_s + \varphi c_{p_{air}}\rho_{air}}{[1-\varphi]\rho_s + \varphi\rho_{air}} \qquad (8)$$

$$k_{powder} = (1-\varphi)^2 k \qquad (9)$$

The subscript $(\,)_{air}$ in (8) and (9) stands for air thermal and physical properties.

Boundary conditions

The overall geometry of the computational domain is shown in **Figure 1**. The domain sizes are 3 mm by 1.5 mm by 1.5 mm and according to this figure, to reduce the computational efforts, the symmetry boundary condition has been imposed on the right face for both thermal and fluid flow calculations. It is assumed that a layer of powder with 20 µm thickness is laid on the bulk material, as shown in **Figure 1**.

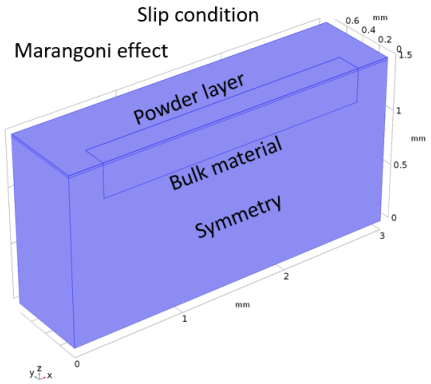

Figure 1. Numerical model and applied boundary conditions.

Based on **Figure 1**, the top boundary is subjected to thermally-induced shear stresses along with a slip-wall boundary.

$$\tau_{zx}|_{top} = \nabla T_x \cdot \frac{d\sigma}{dT}, \qquad (10)$$

$$\tau_{zy}|_{top} = \nabla T_y \cdot \frac{d\sigma}{dT}, \qquad (11)$$

$$w|_{top} = 0\,. \qquad (12)$$

According to equations (10) and (11), the shear stresses on the top surface are dependent on the corresponding temperature gradient. σ $[\frac{N}{m}]$ is the surface tension of the fluid and the last term on the right side of equations (10) and (11) is the temperature-dependent factor of the surface tension. The slip-wall boundary condition in equation (12) shows that the velocity component normal to the top surface is zero, while the two other velocity components are non-zero at this face. Moreover, the thermal boundary condition imposed on the top boundary is a combination of convection and radiation.

$$-k\frac{dT}{dz} = h_{amb}[T - T_{amb}] + \varepsilon\sigma[T^4 - T_{amb}^4] \quad (13)$$

$h_{amb}\ [\frac{W}{m^2.K}]$, $\varepsilon\ [-]$ and $\sigma\ \left[\frac{W}{m^4.K}\right]$ are convective heat transfer coefficient, surface emissivity of the metal and the Stefan-Boltzmann constant respectively.

The heat generation term mentioned in equation (5) is assumed to have a conical shape in the vertical direction and a Gaussian distribution in the plane.

$$\dot{Q}''' = \frac{\alpha.P}{S.\pi.R^2} e^{-2\left(\frac{x^2+y^2}{R^2}\right)} \cdot [1 - \frac{z^+}{S}] \quad (14)$$

$\alpha\ [-]$ and $P\ [W]$ are the laser absorption coefficient and its total power. $z^+\ [m]$ is the vertical coordinate from the top plane downwards. The parameter $S\ [m]$ is the penetration depth of the laser into the material. The domain is meshed with 803966 elements with smallest size of 5 µm.

Results and discussion

Validation

The thermo-physical properties of Ti6Al4V used for numerical modelling are in **Table 1**.

Table 1. Ti6Al4V thermo-physical properties [4], [6].

Property	Value	Property	Value
$k_s\ [\frac{W}{m.K}]$	13	$\frac{d\sigma}{dT}$	-1.6e-4
$k_l\ [\frac{W}{m.K}]$	33	$\mu\ [Pa.s]$	0.005
$Cp_s\ \left[\frac{W}{m.K}\right]$	543	$\beta\ \left[\frac{1}{K}\right]$	1.1e-5
$Cp_l\ \left[\frac{W}{m.K}\right]$	750	$T_s\ [K]$	1893
$LH\ [\frac{kJ}{kg}]$	280	$T_l\ [K]$	1928
$\rho_s\ [\frac{kg}{m^3}]$	4510	$\alpha\ [-]$	0.3

The laser specifications are chosen based on the references [11], [12] for LSNF-1 machine and are gathered in **Table 2.**

Table 2. laser specifications for validation.

$P\ [W]$	$R\ [\mu m]$	$U_{las}\ [\frac{mm}{s}]$	$layer\ thikness\ [\mu m]$
200	50	300	20

The simulation run for 20-core machine with total 803966 elements is 25 hours. A comparison between the measured (experimentally from [11]) and calculated melt pool profiles are depicted in **Figure 2**. According to this, the depth and width of the calculated melt pool matches well with the experimental measurements.

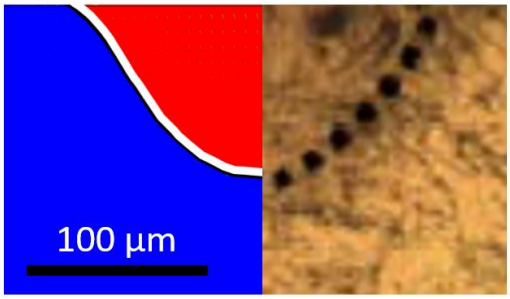

Figure 2. Melt pool cross-sectional profile; (left) numerical model and (right) experimental measurement [11].

Thermal analysis

The temperature contour of the melt pool at t=4 ms is shown in **Figure 3**. And it is observed that the melt pool has a narrow tail at its back where the solidification is occurring.

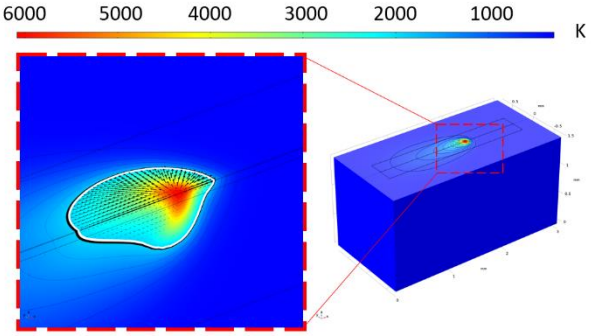

Figure 3. Temperature and melt pool at t=4ms.

The maximum melt pool temperature according to **Figure 3**, is around 6000 K and this peak temperature occurs close to the center of the moving heat source. The melt pool borders as well as the isotherms of liquid and solid temperatures are shown in white and black lines in **Figure 3**.

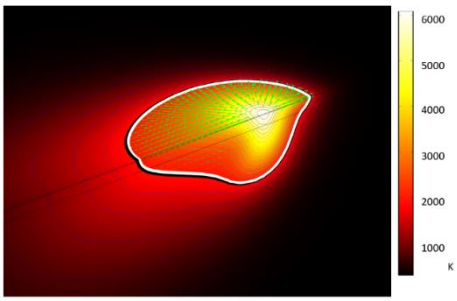

Figure 4. Temperature profile along with the isothermal lines at t=4 ms.

In **Figure 4** it is observed that the temperature isotherms are highly condensed in front of the melt pool, while they are less concentrated at its back. The underlying reason is that the powder has much lower conductivity compared with the bulk material. In this regard, it plays the role of a thermal barrier to the incoming heat fluxes being propagated from the melt pool's center. On the other hand, when fully melted, the powder turns into a bulk and dense material with normal conductivity. Consequently, this will let the heat waves being propagated on the rear side of the melt pool's center to overtly move in the backward direction, since much lower thermal resistance is faced compared to the powder layer.

When the laser starts to contact the material, because of latent heat of fusion of the metal, it takes about 2 ms for melting the part. When the melting starts, initially, between t= 5 to 10 ms, the melt pool grows in depth while its x and y profile are almost symmetric, as shown in **Figure 5**. This is largely because of the fact that, within that 5 to 10 milliseconds, the laser has not moved a discernable distance. In this regard, the melt pool will be almost symmetric and grows equally (isotropic) in x and y directions. However, as time passes, the melt pool becomes elongated in the x direction due to the movement of laser and the same time it grows its size in both y and z directions as well.

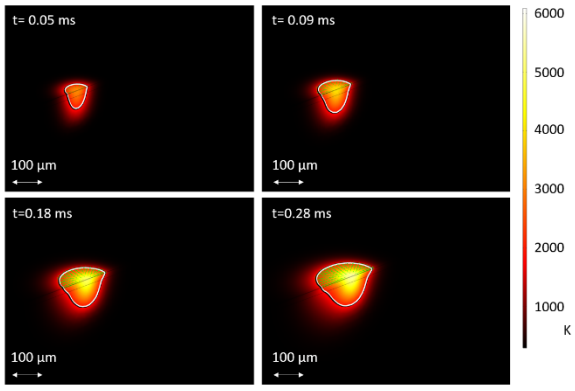

Figure 5. melt pool temperature for the initial phase of the melting during 0.05 ms to 0.28 ms.

The peak temperature of the melt pool increases dramatically by time. To better show this, the temperature profile for the scanning line at different times during the SLM process has been plotted against the x coordinate in **Figure 6**. According to **Figure 6**, within just 0.06 ms, the peak temperature rises to 3500 K and in 0.30 ms it reaches to a substantial amount of 5000 K.

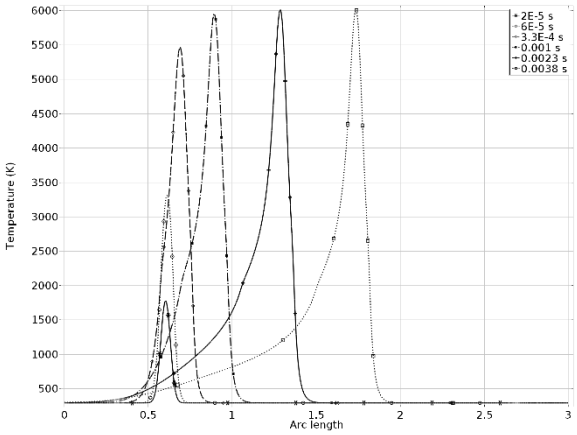

Figure 6. T-x profile for the central scanning line at z=1.5 mm.

On the other side, based on **Figure 6** it is observed that the peak temperature after 1 ms where it reaches the level of 6000 K, remains almost constant until the end of the track. Accordingly, the melt pool reaches a so-called pseudo-steady condition. In this condition, the rate of change of internal energy will get balances with the laser input energy and the ambient radiation.

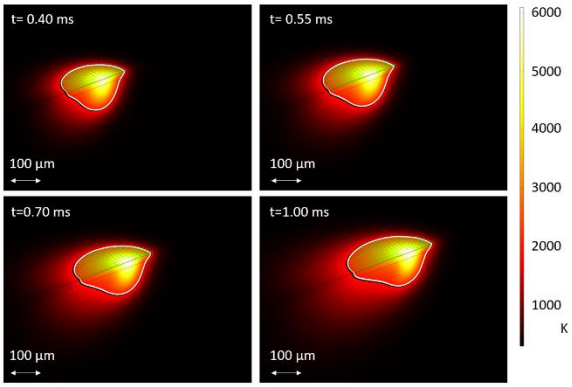

Figure 7. melt pool temperature for the initial phase of the melting during 0.05 ms to 0.28 ms.

The temperature contour of the domain for t=0.40 to 1.00 ms is depicted in **Figure 7**. According to this figure, after 1 ms, the melt pool's morphology will become constant as it reaches the pseudo-steady state condition. From this time on, the size and morphology of the melt pool does not change and its shape will remain constant as well.

What is interesting here is that the mentioned pseudo-steady condition is also observed in the heating/cooling curves shown in **Figure 8**. Based on this figure, the heating rate is about 8e7 K/s initially and it decreases to the level of 2e7 K/s at t=1.00 ms. From this time, the heating rate in front of the melt pool will remain constant as well.

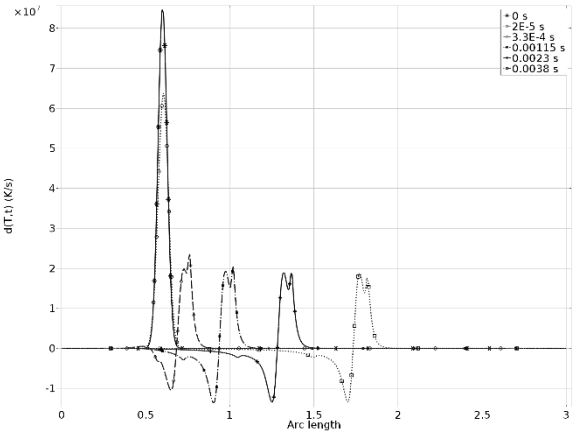

Figure 8. Rate of change of temperature on the central line at z=1.5 mm.

Another interesting feature of **Figure 8** is the formation of two distinct heating and cooling sections on the front and back of the melt pool.

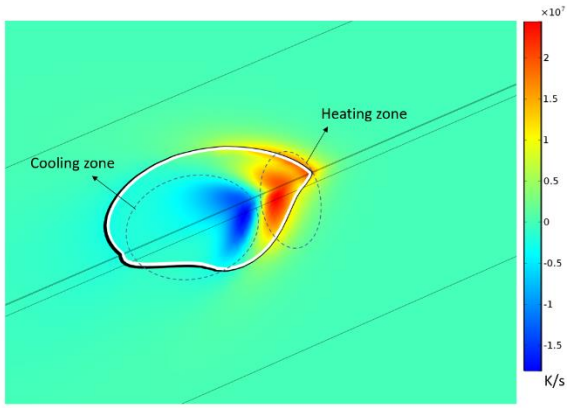

Figure 9. rate of change of temperature inside the melt pool at t=4 ms.

The contour of rate of change of temperature inside the melt pool has been depicted in **Figure 9**. Based on this figure, the rate of change of temperature on the frontal section of the melt pool is a positive value while on its rear section is negative. Also the maximum value of heating rate is around 50 % higher than that of the cooling rate. According to **Figure 9**, one can say that the temperature in the frontal zone of the melt pool is lower than the peak temperature (since it is being warmed up, based on **Figure 6**) and in this way a negative temperature gradient will prevail on this zone. Consequently, with the same logic, a positive temperature gradient site would also appear on the back of the melt pool. The sign of these thermal gradients as will be discussed in the following sections, highly affects the fluid flow inside the melt pool.

Fluid flow inside the melt pool

The melt pool's cross-section in the xz plane at y=0 has been shown in **Figure 10** along with the liquid fraction contour.

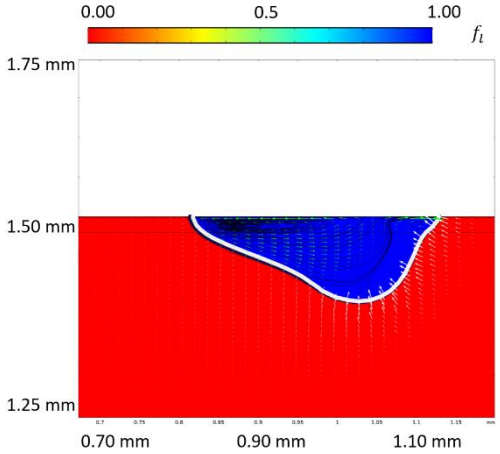

Figure 10. Melt pool profile in the central xz plane along with liquid fraction contour.

In **Figure 10** the stream lines are shown in black and the temperature gradient vectors are shown in white arrows. The velocity vectors are shown in green arrows. According to **Figure 10**, the temperature gradient lines are all perpendicular to the liquid and solidus lines. More importantly, it is clearly observed that two circulations are formed on the two sides of the melt pool. While the melt pool is pushing forward, since it faces resistance from the mushy zone, a much smaller circulation will form in the frontal zone. However, since the melt pool is well-elongated backwards, the rear circulation is much bigger.

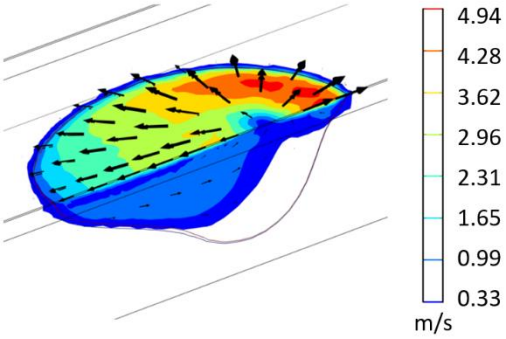

Figure 11. 3D visualization of the melt pool along with iso-surfaces for velocity.

For better understanding of the velocity profile, velocity iso-surfaces are shown in **Figure 11**. The frontal zone has higher maximum velocity which is due to the fact that on

this zone a very high temperature gradient exists which will prompt a strong flow because of the Marangoni effect. The process conditions calculated during the solidification process on the y-z plane a x=1.4 mm during the single track SLM process are gathered in **Figure 12**.

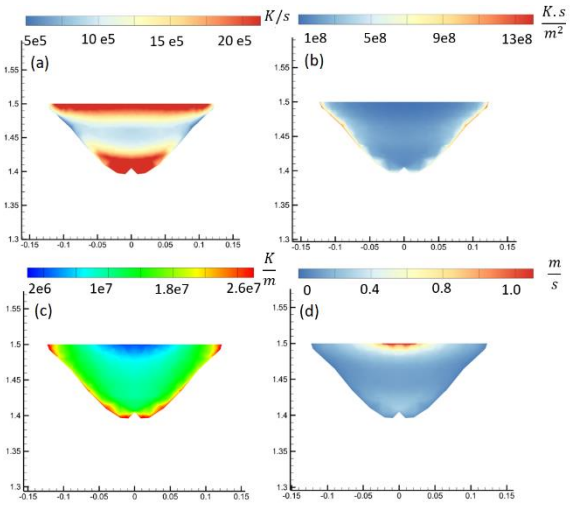

Figure 12. Contour of: (a) cooling rate, (b) morphology factor, (c) thermal gradient and (d) growth velocity during the solidification in yz plane at x=1.4 mm.

The solidification cooling rate on the yz plane are plotted in **Figure 12** (a). Based on this figure, the maximum cooling rates occur both at the bottom and top of the initial melt pool profile, in which the solidification of that cross section starts and ends respectively. The morphology factor contour shown in **Figure 12** (b) has its maximum values at the sides of the initial profile. The higher morphology factor, the higher the probability of formation of planar grains. Also the solidification temperature gradient are calculated and shown in **Figure 12** (c). It is observed that the minimum thermal gradients are formed at the initial melt pool borders, which is consistent with observations made in laser welding as well [13], [14]. The contour of solidification growth velocities shown in **Figure 12** (d) depicts the fact that the maximum growth velocity is obtained at the top of the melt pool where the solidification ends. The maximum value of the growth velocity is 3.8 m/s in this case.

The morphology factor and solidification growth velocities are plotted against time during the solidification of the mentioned section in **Figure 13**.

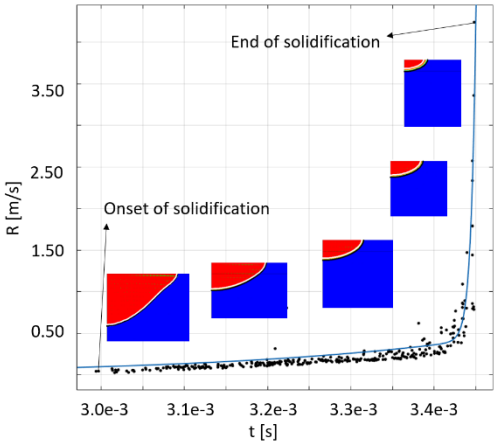

Figure 13. solidification growth velocity vs time for yz cross-section x=1.4 mm.

According to **Figure 13**, the solidification growth speed is initially small and in the order of 0.2 m/s where the melt pool itself is big. As the laser moves forward, the melt pool also moves with it, hence the melt pool shrinks in size in this yz section. Based on **Figure 13**, the solidification growth velocity increases linearly with time until t=3.4 ms. From that point until the end of the solidification process, where the melt pool is very small as well, the solidification growth speed suddenly rises to a maximum amount of 3.8 m/s. This issue is in consistent with the observations made in electron beam welding [15].

Conclusion

In this work a thermo-fluid-metallurgical numerical model for the SLM process has been developed with COMSOL Multiphysics 5.3a. In this model the Marangoni effect is taken into the account. To model the solidification process, the solidification drag forces are used to free and freeze the velocity field, depending upon the liquid fraction. Furthermore a metallurgical model has been developed and subsequently coupled to the thermo-fluid model to extract the four important process conditions. By introducing a Gaussian-conical heat source term, it is shown that the current model can predict the shape and size of the melt pool profile, as the numerical results are in a very good agreement with those of the experimental measurements found in the literature. Furthermore, it is observed that two distinct heating and cooling sections will form respectively in the front and rear of the melt pool, while it moves. Also the results suggest that the peak temperature and the melt pool profile reach a pseudo-steady condition after 1 ms. Moreover, the solidification parameters calculated by means of the metallurgical model show that the growth

velocity rises from a low value of 0.2 m/s at the onset of solidification to a big level of 3.8 m/s at the end of the solidification. Besides, the calculated solidification parameters are found to be in consistent with those found in the literature for laser welding applications as well.

References

[1] T. DebRoy *et al.*, "Additive manufacturing of metallic components – Process, structure and properties," *Prog. Mater. Sci.*, vol. 92, pp. 112–224, 2018.

[2] V. Bhavar, P. Kattire, V. Patil, S. Khot, K. Gujar, and R. Singh, "A review on powder bed fusion technology of metal additive manufacturing," no. September, 2014.

[3] L. E. Criales, Y. M. Arısoy, and T. Özel, "Sensitivity analysis of material and process parameters in finite element modeling of selective laser melting of Inconel 625," *Int. J. Adv. Manuf. Technol.*, vol. 86, no. 9–12, pp. 2653–2666, 2016.

[4] Y. Huang, L. J. Yang, X. Z. Du, and Y. P. Yang, "Finite element analysis of thermal behavior of metal powder during selective laser melting," *Int. J. Therm. Sci.*, vol. 104, pp. 146–157, 2016.

[5] S. Mohanty and J. H. Hattel, "Numerical model based reliability estimation of selective laser melting process," *Phys. Procedia*, vol. 56, pp. 379–389, 2014.

[6] L. Parry, I. A. Ashcroft, and R. D. Wildman, "Understanding the effect of laser scan strategy on residual stress in selective laser melting through thermo-mechanical simulation," *Addit. Manuf.*, vol. 12, pp. 1–15, 2016.

[7] Y. S. Lee and W. Zhang, "Modeling of heat transfer, fluid flow and solidification microstructure of nickel-base superalloy fabricated by laser powder bed fusion," *Addit. Manuf.*, vol. 12, pp. 178–188, 2016.

[8] C. Qiu, C. Panwisawas, M. Ward, H. C. Basoalto, J. W. Brooks, and M. M. Attallah, "On the role of melt flow into the surface structure and porosity development during selective laser melting," *Acta Mater.*, vol. 96, pp. 72–79, 2015.

[9] Z. Gan, H. Liu, S. Li, X. He, and G. Yu, "Modeling of thermal behavior and mass transport in multi-layer laser additive manufacturing of Ni-based alloy on cast iron," *Int. J. Heat Mass Transf.*, vol. 111, pp. 709–722, 2017.

[10] V. R. Voller and C. Prakash, "A fixed grid numerical modelling methodology for convection-diffusion mushy region phase-change problems," *Int. J. Heat Mass Transf.*, vol. 30, no. 8, pp. 1709–1719, 1987.

[11] J. Yang *et al.*, "Role of molten pool mode on formability , microstructure and mechanical properties of selective laser melted Ti-6Al-4V alloy," *JMADE*, vol. 110, pp. 558–570, 2016.

[12] Z. Wang, K. Guan, M. Gao, X. Li, X. Chen, and X. Zeng, "The microstructure and mechanical properties of deposited-IN718 by selective laser melting," *J. Alloys Compd.*, vol. 513, pp. 518–523, 2012.

[13] W. Tan and Y. C. Shin, "Multi-scale modeling of solidification and microstructure development in laser keyhole welding process for austenitic stainless steel," *Comput. Mater. Sci.*, vol. 98, pp. 446–458, 2015.

[14] Z. Gan, G. Yu, X. He, and S. Li, "Numerical simulation of thermal behavior and multicomponent mass transfer in direct laser deposition of Co-base alloy on steel," *Int. J. Heat Mass Transf.*, vol. 104, pp. 28–38, 2017.

[15] N. Raghavan *et al.*, "Acta Materialia Numerical modeling of heat-transfer and the in fl uence of process parameters on tailoring the grain morphology of IN718 in electron beam additive manufacturing *," *Acta Mater.*, vol. 112, pp. 303–314, 2016.